Journal of Materials Chemistry C

PAPER

View Article Online
View Journal | View Issue

Cite this: J. Mater. Chem. C, 2014, 2, 4980

Processing and characterization of cobalt silicide nanoparticle-containing silicon carbide fibers through a colloidal method and their underlying mechanism

Liu Anhua,†* Chen Jianming,† Ding Shaonan, Yao Yanbo, Liu Ling, Li Fengping and Chen Lifu

Received 17th February 2014
Accepted 14th April 2014

DOI: 10.1039/c4tc00315b

www.rsc.org/MaterialsC

Cobalt-containing silicon carbide (Co–SiC) fibers were synthesized through a colloidal method. Dicobalt octacarbonyl [$Co_2(CO)_8$] was employed to react with low-molecular weight liquid polycarbosilane (LPCS) to prepare a stable Co-containing colloid (Co-colloid), which was subsequently added to high-molecular weight solid polycarbosilane to obtain the precursor. FTIR, GPC, XRD, and TEM were employed to further understand and develop the mechanism for the formation of the Co-colloid. Results show that active Co intermediates derived from the incomplete decomposition of $Co_2(CO)_8$ promoted LPCS cross-linkage. The effects of the Co-colloid on the oxidation-curing nature of the green fiber were also investigated. Under heat treatment at higher temperature, carbonyls in the fibers completely decomposed and further crystallized in the morphology of cobalt silicide (CoSi) domains. The effects of Co on the electrical resistivity, magnetic properties, dielectric properties, microwave absorption properties and tensile strength of SiC fibers were also studied.

1. Introduction

Continuous silicon carbide (SiC) fibers are a kind of polycrystalline SiC fibers of high specific strength, high specific modulus, high temperature resistance, oxidation resistance, and chemical corrosion resistance, which also absorb magnetic waves.[1–13] For instance, when their electrical resistivity is in the range of 10^0 Ω cm to 10^3 Ω cm, they absorb the most amount of radar waves in the X-ray wave band.[3,14] Thus, they can be used as reinforcing fibers in high temperature-resistant, structural wave-absorbing composite materials combining structure and function, which have important applications in the field of aviation and aerospace.[15]

For a material to absorb electromagnetic waves, electrical loss and magnetic loss have dominant functions in energy dissipation. Relatively low electrical resistivity and high magnetism are required to endow SiC fibers with good wave absorbance. Theoretical and experimental studies have proven that introducing metals (*i.e.*, Al, Ti, Zr, Hf, Fe, Co, and Ni) into SiC fibers is very effective in promoting or even in endowing them with more outstanding electromagnetic performance.[3–10] Among various additives, elemental Fe, Co, and Ni are undoubtedly better choices over other transition metals in the wave-absorbing field because they can increase not only the electrical conductivity, but also the magnetism. Other metallic compounds, such as Al, Zr, or Ti, are only able to decrease the electrical resistance. General synthesis of transition metal-enhanced, polymer-derived ceramics (PDCs) can be briefly divided into two categories.[16] First, the precursor is physically blended with metal or metal oxide powders. This simple blend method can be used to manufacture PDCs,[17–19] but cannot be used to fabricate continuous SiC fibers containing transition metals because of their poor dispersion, interface interaction, and particle sizes.[20] Second, the chemically modified precursor polymers are synthesized using coordination compounds, in which the metal atoms have already bonded to the monomer units before polymerization.[21,22] This method usually leads precursors to crosslink and improve the ceramic yield, making this strategy suitable for producing PDC containing transition metals. However, it is not the first choice in producing transition metal-modified ceramic fibers because the over-cross-linking makes precursors difficult to spin or even unspinnable. Early in 1981, Smith invented a colloidal method to prepare homogeneous and physically stable polymer-bound Co particles having an average size between 1 and 20 nm.[23] The three essential elements in this approach consist of cobalt carbonyl, active polymer, and inert solvent. Inspired by this colloidal route, utilizing "active" polycarbosilane (PCS) to react with a kind of metal carbonyl to obtain a uniformly dispersed

Advanced Materials Laboratory, Key Laboratory of High Performance Ceramic Fibers of Ministry of Education, College of Materials, Xiamen University, Xiamen 361005, China. E-mail: ahliu@xmu.edu.cn

† These authors contributed equally to this work and should be considered co-first authors.

nanoparticle, a metal-containing precursor, and Fe–SiC fibers seems possible; thus, the process was carried out accordingly.[24]

Potential applications of these as-prepared Fe–SiC fibers may be limited at low temperatures because of the low Curie point (~770 °C). High temperature-resistant components of stealth aircraft (*e.g.*, turbine engine with high thrust–weight ratio) have specific needs for high temperature-resistant, wave-absorbing SiC fibers. Thus, developing high temperature, wave-absorbing SiC fibers has profound significance. Compared with Fe and Ni, Co has a much higher Curie point (~1150 °C), which allows cobalt-containing SiC (Co–SiC) fibers to protect their magnetic properties from destruction at higher temperatures. Therefore, SiC fibers containing Co have great potential to be used as reinforcing fibers of high temperature-resistant composite components of stealth aircraft.

In this work, Co will be introduced to the SiC fibers through the above mentioned colloidal route for the first time. Choosing the colloidal method is mainly based on two considerations. First, during the preparation of the colloid, the active metallic compounds react with low-molecular weight PCS (LPCS), resulting in the loss of its reactivity. Thus, in the following blending and spinning processes, the reaction with spinnable PCS to form highly crosslinked resultants can be avoided. This condition is the key to introduce metallic Co into SiC fibers successfully. Second, the nano-sized colloid that is mutually soluble with spinnable PCS can be uniformly dispersed in it. Metallic nanoparticles can also be uniformly dispersed among the crystalline grains of SiC fibers. According to these concepts, the colloidal method can also be applied to prepare other ceramic fiber containing metals. Fourier transform infrared spectroscopy (FTIR), gel permeation chromatography (GPC), X-ray diffraction (XRD), and transmission electron microscopy (TEM) are employed to further understand and develop the mechanism for the formation of a Co-containing colloid (Co-colloid). An oxygen–nitrogen analyzer, Soxhlet extraction, and FTIR are combined to study the distinctive oxidation performance of Co-containing green fibers. XRD and TEM are applied to study the mechanism of the microstructure evolution during the process of pyrolysis and the effect of Co on the mechanical and microwave absorption properties.

2. Experimental procedure

2.1. Preparation of PCS

PCS was synthesized following the work described in the literature.[25,26] Polydimethylsilane $[Si(CH_3)_2]_n$ was first heated at a high temperature and converted into PCS through Kumuda rearrangements.[27,28] PCS was then dissolved and filtered to remove the impurity. After vacuum drying, the PCS was vacuum distilled into two portions: LPCS (*i.e.*, liquid, semi-viscous, and transparent at room temperature) and high-molecular weight PCS (*i.e.*, yellowish solid at room temperature; HPCS). The elementary compositions and molecular weights of LPCS and HPCS are shown in Table 1.

Table 1 Properties of LPCS, HPCS, and Co-colloid

Material	Co (wt%)	C (wt%)	O (wt%)	Si (wt%)	H (wt%)	$\overline{M_n}$
LPCS	—	40.53	0.74	51.13	7.60	320
HPCS	—	41.67	0.71	51.51	6.11	1220
Co-colloid	28.83	25.86	22.13	20.03	3.15	730

2.2. Preparation of the Co-colloid

Dicobalt octacarbonyl [$Co_2(CO)_8$, 95%] was purchased from Strem Chemicals, Inc. (Poison Center, U.S.A.). Under Ar (99.9999%), $Co_2(CO)_8$ was dissolved together with LPCS in decalin ($C_{10}H_{18}$, 99.5%) on the basis of the mass ratio $Co_2(CO)_8$: LPCS : $C_{10}H_{18}$ = 1 : 0.8 : 40, forming a dark brown solution. After heating to reflux for 7 h, a black Co-colloid was finally obtained. The Co-colloid was highly stable without precipitation even after a few months. By contrast, the resultant suspension sank quickly onto the bottom of the container in the absence of LPCS. After vacuum distillation at 140 °C, the liquids with or without LPCS were both converted to black powders for chemical analysis and phase identification. Table 1 shows the chemical composition and average molecular weight of the Co-colloid.

2.3. Preparation of Co–SiC fibers

The Co-colloid and HPCS were dissolved in xylene to obtain a viscous and homogeneous black solution. After vacuum distillation at 120 °C, Co-precursor powders were prepared for melt-spinning. Precursors containing nominal Co contents of 0 and 1 wt% were called PCS and Co–PCS, respectively. A laboratory melt-spinning machine (MMCH05, Chemat, Northridge, CA) was used for the melt-spinning of precursor fibers. Under Ar, the precursor was heated to the set temperature (~310 °C). The molten polymer was then extruded through a single-hole spinneret. The diameter of the orifice was 0.3 mm. Precursor fibers were collected on the winding bobbin at a winding speed of 450 m min^{-1}. The as-spun fibers were cut into 60 mm lengths and ~0.5 g was placed into a tube furnace (inner diameter = 35 mm). They were oxidized at 280 °C in dry air flowing at 200 cm^3 min^{-1}. The heating rate was 10 °C h^{-1} and the holding time was 5 h. The cured fibers were placed into a perforated graphite boat. They were then pyrolyzed in high-purity nitrogen (99.999%) to the set temperature. The heating rate was 5 °C min^{-1} and the holding time was 10 min.

2.4. Analysis and characterization

FTIR spectra that were used to identify groups were recorded on a Nicolet Avator 360 (Nicolet, Madison, WI) with KBr plates for liquid samples and KBr disks for solid samples. The molecular weight and its distribution were measured by GPC (Agilent 1100 system, Agilent, Palo Alto, CA). The analysis was performed at 35 °C with tetrahydrofuran as the eluent (1.0 mL min^{-1}) and narrow-molecular weight distribution polystyrene as the standard. Thermal analysis was performed under flowing N and at a

heating rate of 10 °C min^{-1} (TA, Netzsch STA 409, Netzsch, Selb, Germany).

C and O contents were determined using a carbon–sulfur analyzer (EMIA-320V, Horiba, Kyoto, Japan) and an oxygen–nitrogen analyzer (EMGA-620W, Horiba), respectively. The Co content was quantitatively measured by using an ultraviolet-visible absorption spectrometer.[29] At least five tests were conducted for each point, and the average value was used. The relative errors were 1.2%, 0.9%, and 2% for C, O, and Co, respectively. The silicon content was determined through the difference method. The tensile strength and elastic modulus of the SiC fibers were measured using a tensile-testing machine (YG(B)003A, Wenzhou Darong Textile Instrument Co., Ltd., Zhejiang, China). The gauge length was 25 mm and the cross-head speed was 1 mm min^{-1}. At least 20 effective measurements were conducted, and the average value was used.

SEM (XL30, Philips-FEI, Eindhoven, Netherlands) was used to determine the fiber diameter and surface morphology. TEM (Tecnai F30, Philips-FEI) was performed for microstructure observation. XRD (PANalytical X'Pert PRO diffractometer, PANalytical, Almelo, Netherlands) was carried out for phase identification. A vibrating sample magnetometer (VSM; LakeShore-7404, USA) was used to examine the magnetic properties. An automatic bridge meter (LCR; HP-4284A, USA) was used to measure the electrical resistivity. The relative complex permittivities of samples with dimensions of 22.86 × 10.16 × 2.5 mm^3 were measured using the vector network analyzer (VNA, MS4644A, Japan) in the frequency range 8.2–12.4 GHz (X band) according to ASTM D 5568-08.

3. Results and discussion

3.1. Underlying formation mechanism of the Co-colloid

The FTIR spectra of LPCS and HPCS are shown in Fig. 1(a) and (b), respectively. Although LPCS and HPCS differ in molecular weight (as shown in Table 1), they are nearly the same with regard to the chemical groups. As reported by other researchers,[30,31] absorption peaks at 1020 and 1355 cm^{-1} are attributed to Si–CH_2–Si, 2950 cm^{-1} to CH_3, 2900 cm^{-1} to CH_2, 2100 cm^{-1} to Si–H, 1250 cm^{-1} to Si–CH_3, and 830 cm^{-1} to Si–CH_3. The absorption peaks centered at 2000 and 1823 cm^{-1} are ascribed to the vibration of C═O groups in $Co_2(CO)_8$, as shown in Fig. 1d.[32,33] After reacting with LPCS, the original C═O group peaks disappear and shift to the lower wavenumber (*i.e.*, 1582 cm^{-1}) of the Co-colloid (Fig. 1c), indicating that the organic Co compound has not yet completely decomposed and produced carbonyl complexes.[23,24] Notably, the peak intensity of the Co-colloid at about 1000 cm^{-1} which is assigned to the Si–O or Si–C group is also noticeably enhanced. The peak intensity of the Si–H group is extremely weakened in the colloid. The molecular weights of LPCS and Co-colloid were characterized by GPC. The results are depicted in Fig. 2 and Table 1. The molecular weight of the colloid is clearly higher than that of the LPCS. The FTIR and GPC results indicate that the Si–H bond reacted with $Co_2(CO)_8$ in the colloidal processing, coupling with the fabrication of multinucleate carbonyls and cross-linked PCS.

The decomposition product of $Co_2(CO)_8$ in decalin under the same conditions but without LPCS is also investigated in contrast to dried Co-colloid powders. The XRD pattern is shown in Fig. 3. The characteristic peak (Fig. 3b) of α-Co at 44.5° is detected because of the complete decomposition of $Co_2(CO)_8$. However, Co-colloid powders are amorphous and no obvious diffraction peaks (Fig. 3a) are observed. The results demonstrate that the decomposition of $Co_2(CO)_8$ is retarded in the presence of LPCS, which is consistent with the conclusion obtained from the FTIR results. In the TEM micrograph of the Co-colloid (Fig. 4), the black particles are cobalt and the light nanoparticles are PCS. The unevenness gathered cobalt in the colloid results in the hollow kind nanoparticles. Colloidal particles have a narrow distribution (3–10 nm) and are uniformly dispersed in the solution matrix. The average size of the nanoparticles is 7 nm.

According to the FTIR, GPC, XRD, and TEM results, as well as other published studies,[23,24,32–36] we attempted to understand the formation mechanism of the Co-colloid. At first, along with the increased reaction temperature and prolonged reaction

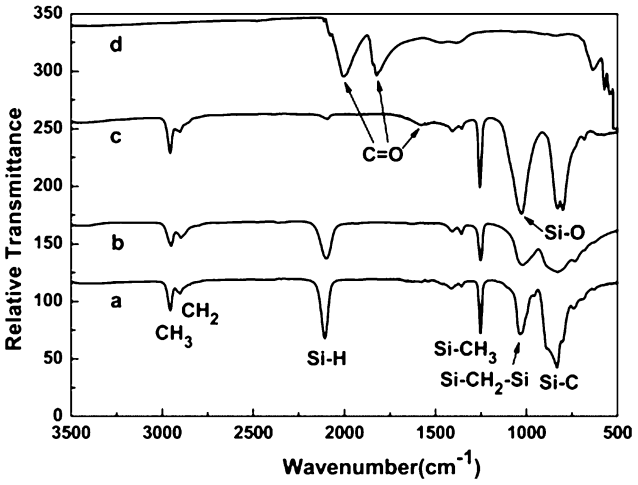

Fig. 1 FTIR spectra of (a) LPCS, (b) HPCS, (c) Co-colloid, and (d) $Co_2(CO)_8$.

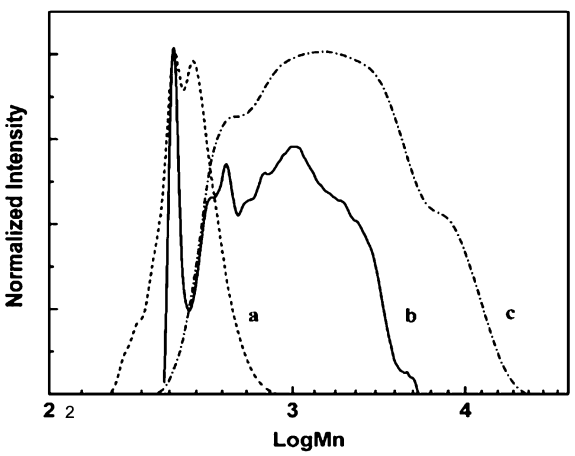

Fig. 2 GPC curves of (a) LPCS, (b) Co-colloid, and (c) HPCS.

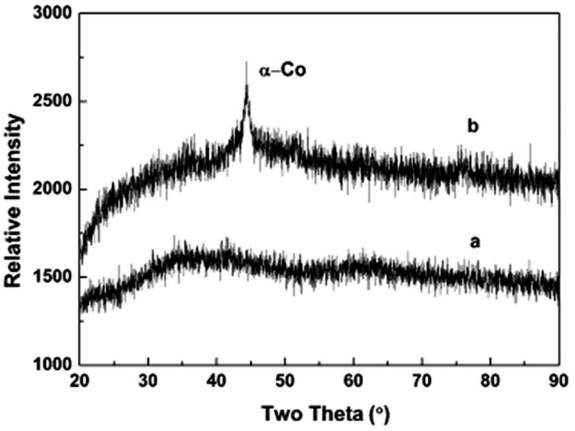

Fig. 3 XRD profiles of (a) Co-colloid powders and (b) decomposition product of $Co_2(CO)_8$ without LPCS.

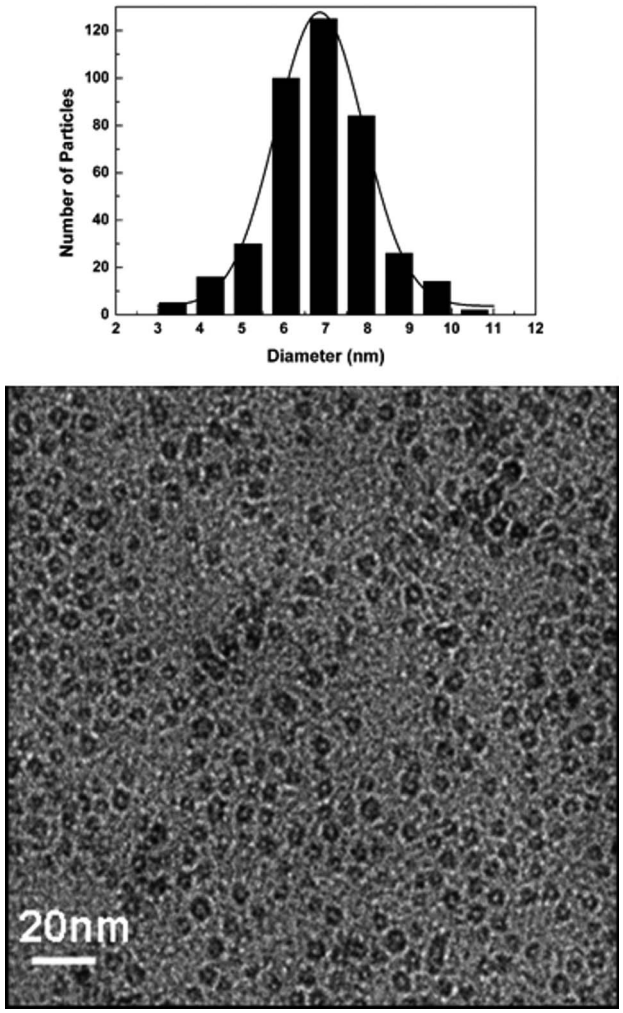

Fig. 4 TEM micrograph of the Co-colloid and particle size histogram of the corresponding TEM.

time, carbonyl cobalt decomposes into active intermediates, such as [Co $(CO)_4$] or [Co $(CO)_3$], and simultaneously release CO. These intermediates are chemically unstable, which react randomly with each other to liberate more CO gas and produce varieties of relatively stable carbonyl complexes, such as $Co_4(CO)_{12}$. Corriu *et al.*[37] believed that active Co intermediates (or [Co]) induce a catalytic effect on the cleavage of C–H bonds or even Si–C bonds in the matrix, resulting in the cross-linked structure of [–Si–CH_2–Si–] at a lower temperature with free radical reaction. Except for the C–H bonds and Si–C bonds, LPCS consists of abundant and active Si–H bonds. During the preparation of the Co-colloid, Si–H bonds in the LPCS will be preferentially catalyzed by [Co] and then become cross-linked to form Si–CH_2–Si and Si–O–Si bonds.

The formation of the Si–CH_2–Si and Si–O–Si bonds is in good agreement with the conclusion obtained from the FTIR, GPC, XRD, and TEM results. During the formation of the Co-colloid, $Co_2(CO)_8$ first incompletely decomposes into multinucleate carbonyl particles and CO. The LPCS then becomes cross-linked after reacting with the evolved CO. Finally, nano-sized carbonyl particles (the "core") are encapsulated by cross-linked LPCS (the "shell"), thus forming the colloid with PCS-bounded Co particles. The core–shell structure not only hinders the evolution of CO, but also impedes further decomposition of carbonyls into Co.[16]

3.2. Processing of Co–SiC fibers

The dried colloid powder, in which the Co content is up to 28.83 wt% (Table 1), is insoluble and unable to melt-spin. When it is blended into HPCS, the as-prepared precursor obtains various spinning performances with different Co contents. As the Co content increases, the melt-spinning ability of the precursor clearly deteriorates. Making a trade-off between the Co content and the melt-spinning ability of the precursor, as well as the properties of the resultant SiC fiber, is necessary. In this paper, we mainly focus our attention on the Co–PCS with ~1 wt% Co content.

Fig. 5 shows the GPC curves of the Co–PCS precursor and as-spun fibers. The GPC pattern (Fig. 5a) of the Co–PCS precursor is analogous to that of the HPCS (Fig. 2). However, after spinning, a new band corresponding to a higher molecular weight ($\sim M_n = 10^{5.3}$) appears on the curve (Fig. 5b) of as-spun Co–PCS fibers. The result is probably caused by the sample being heated

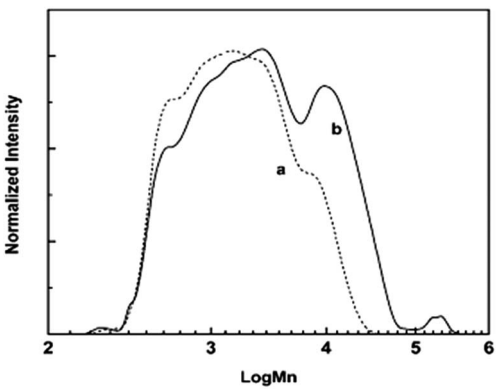

Fig. 5 GPC curves of the (a) Co–PCS precursor and (b) as-spun Co–PCS fibers.

at a molten state for at least 3 h to expel the air under vacuum before spinning. During this holding period, the temperature is sufficiently high to activate the Si–H groups in the HPCS and the incompletely decomposed carbonyls. The Si–H groups then continue to take part in the free radical reaction and oxidized addition reaction, resulting in the formation of higher-molecular weight polymers. The as-spun fiber is smooth, dense, and free of large defects.

Before pyrolysis, the oxidation-curing step is usually performed to prevent the green fibers from fusing. According to the literature,[38,39] PCS fibers are normally cured in the range of 150 °C to 200 °C for more than 10 h, and at least 8 wt% oxygen content is expected. As shown in Fig. 6, Co–PCS fibers tend to be less sensitive to temperature than the control sample. The oxygen content increases slowly even as the temperature is up to a relatively high value. Making the oxygen content tunable in a limited range is easy and convenient. In contrast to pure HPCS fibers, the oxygen content of Co–PCS fibers is only 5.05%, although the temperature is as high as 280 °C. Given these conditions, the low oxidative activity of Co–PCS fibers may be due to the addition of the colloid.

The detection of the gel content is conducted for the cured Co–PCS fibers by Soxhlet extraction. As shown in Fig. 6, the plot of the gel content remains steady, and the values are about 0 below 250 °C, followed by a noticeable rise between 250 and 280 °C, and then back to stable from 280 °C onward. The deviation is probably caused by the HPCS in the Co–PCS precursor being involved in the crosslink reaction in the melt-spinning stage. Turning to the oxidation stage, the diluted Si–H bonds and the crosslink structure in the Co–PCS fibers exhibit a negative trend to the formation of Si–OH groups, as well as the effective "collision" between them. Compared with the HPCS fibers, the Co–PCS fibers have to be cured at a much higher temperature because of a lower oxidation activity.

The Co–PCS fibers were characterized by FTIR to obtain a more comprehensive understanding of the oxidation mechanism. According to a previous report,[40] Si–OH groups predominantly originate from the oxidation of abundant and active Si–H bonds, and only at a higher temperature could the Si–CH_3 groups be oxidized with C=O bonds. Finally, the PCS becomes cross-linked with the Si–O–Si bonds formed by a combination of the Si–OH groups. As shown in Fig. 7, Si–OH and C=O groups are observed at 3680 and 1710 cm^{-1}, respectively. When the temperature increases from 250 °C to 280 °C, the relative peak intensities of Si–H and Si–CH_3 groups decline sharply, whereas those of the Si–O–Si bonds exhibit the opposite trend. During the oxidation of the Co–PCS fibers, the Si–H bonds are first oxidized at low temperatures and then arrive at the synergistic oxidation of Si–H and Si–CH_3 groups at high temperatures. The experiment results show that the shape of the Co–PCS fibers is kept intact when the gel content is higher than or equal to 55.5% (at 270 °C). In this work, the Co–PCS fibers were selected to be cured at 280 °C for 5 h without the risk of fusion.

The crystallographic development of Co–SiC fibers during heat treatment is shown in Fig. 8. At 900 °C, a sharp peak emerging at 26.7° is considered to be the (002) lattice plane of C. Three peaks appearing at $2\theta = 35.6°$, 60.0°, and 72.0° at 1000 °C are also attributed to the (111), (220), and (311) planes of β-SiC, respectively. Minor but clear and broad bands are also centered at 45.6° and 50.2° at 1100 °C, corresponding to the (210) and (211) planes of CoSi. All peaks become sharper as the pyrolysis temperature increases because of the increased degree of crystallization.

According to the XRD results and the literature,[41,42] the dominant crystalline morphology of Co in the SiC fibers is CoSi, and the formation of CoSi is described as follows:

$$2Co + SiC \rightarrow Co_2Si + C$$

$$Co_2Si + SiC \rightarrow 2CoSi + C$$

$$Co + SiC \rightarrow CoSi + C$$

Co_2Si and CoSi are classified as two typical Co silicides. The former could not exist above 900 °C, which is also in line with the XRD results. CoSi, normally known as a promising

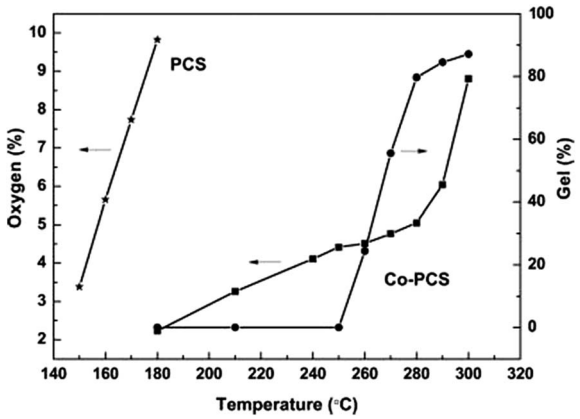

Fig. 6 Oxygen content of PCS (★), Co–PCS (■), and gel content of Co–PCS (●) at different oxidation temperatures.

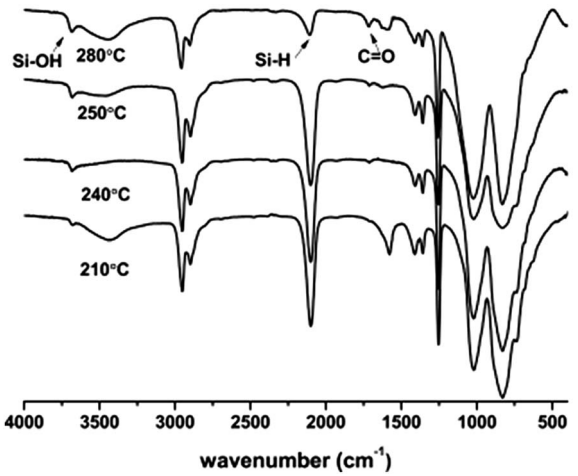

Fig. 7 FTIR spectra of Co–PCS fibers at different oxidation temperatures.

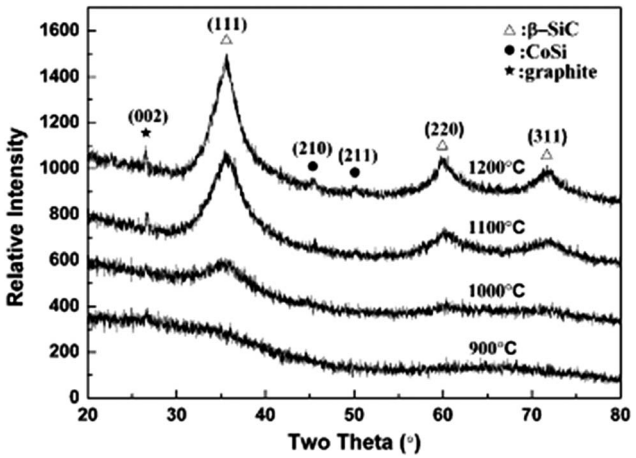

Fig. 8 XRD profiles of Co–SiC fibers (curing temperature = 280 °C).

intermetallic compound, possesses low electrical resistivity, excellent oxidation resistance, and high thermal and chemical stabilities.[38,39] In addition to the formation of CoSi, C originating from the PCS is also the main product that may contribute to the crystallization of graphite-like C.

At 1200 °C, the Co–SiC fibers consist of β-SiC grains with an average size of 9.4 nm. β-SiC grains in the Co–SiC fibers are much larger than the PCS-derived SiC fibers without Co, such as Nicalon (Nippon Carbon Co. Ltd., Tokyo, Japan), where the β-SiC crystallized to 2 nm to 3 nm.[43,44] The deviation was probably caused by the Co or liquid phase of Co–Si–(C) formed at a high temperature being catalytic and effective for the nucleation and growth of the β-SiC crystallites.[13,45,46]

Fig. 9 shows the TEM image of the Co–SiC fibers at 1200 °C. The radii of the electron diffraction rings (Fig. 9, inset) are measured to verify the presence of CoSi and β-SiC grains. The results are in line with the XRD patterns. As shown in Fig. 9, β-SiC is detected and uniformly dispersed in the amorphous SiC_xO_y matrix, along with the graphite-like C. The CoSi grains are wrapped by a large amount of C and β-SiC phases, which can hardly be detected by measuring the interplanar distance.

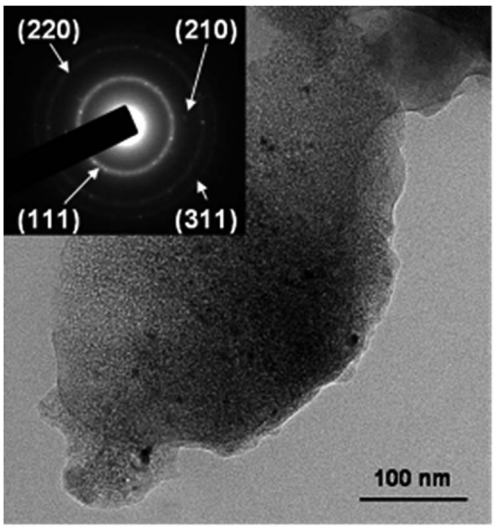

Fig. 9 TEM micrograph of Co–SiC fibers for curing at 280 °C and pyrolysis at 1200 °C. The electron diffraction ring of Co–SiC fibers (inset).

Table 2 shows the average size of CoSi (D_{CoSi}), Co content (Co%), electrical resistivity, saturation magnetization, coercivity, and ceramic yield at different pyrolysis temperatures. CoSi forms at 1100 °C with an average size of 12.2 nm. The present Co% in the final ceramic fibers is slightly higher than the nominal Co content (1 wt%) in the precursors. As CoSi emerges at 1100 °C, its corresponding resistivity remarkably declines, and the lowest resistivity (17.68 Ω cm) is obtained at 1200 °C. The resistivity drops sharply from 1000 °C to 1100 °C, correlating well with the improved crystallization degree of β-SiC and C phases and the formation of the CoSi phase.[47] Electrical resistivity ranging from 0 Ω cm to 1000 Ω cm has been studied to be effective in electromagnetic wave absorption.[6,8] As depicted in Table 2, a Co–SiC fiber of ~1 wt% Co content could be regarded as a good candidate to be applied in the absorbing field within the specific temperature range. The ceramic fibers have saturation magnetization and coercivity ranging from 0.7653 to 0.0062 emu g^{-1} and from 8.74 to 112.77 G, respectively.

Fig. 10 shows the hysteresis loop of the Co–SiC fibers. As the pyrolysis temperature increases, the development tendency of the saturation magnetization and coercivity shows the exact opposite pattern. For example, the saturation magnetization is the highest (0.77 emu g^{-1}) at 900 °C, whereas the corresponding coercivity is the lowest (8.74 G). From the magnetic parameters in Table 2, the as-prepared Co–SiC fibers belong to soft magnetic materials. As the temperature increases, CoSi crystallites become perfect, and then the magnetism disappears. The hysteresis loop presenting a strong trend of diamagnetism with a better crystallized CoSi at 1200 °C becomes fairly apparent.

The relative complex permittivity ($\varepsilon = \varepsilon' - j\varepsilon''$) is the key parameter for the characterization of the dielectric properties, prediction and design of the microwave absorption properties of the materials. The real permittivity (ε') represents the polarization relaxation and the imaginary permittivity (ε'') represents the dielectric loss of the materials. The real permittivities of Co–SiC fibers are shown in Fig. 11(a). Obviously, the real permittivities of all samples increase with the increase of pyrolysis temperature, which is the same for the imaginary permittivities as shown in Fig. 11(b). The loss tangent represents the microwave attenuation properties of materials. Higher tan δ means better microwave attenuation properties. Fig. 11c shows the variation of loss tangent as a function of pyrolysis temperature. The loss tangents of Co–SiC fibers also increase with rising temperature, indicating that microwave attenuation properties increase with the increase of the pyrolysis temperature. Therefore, with rising temperature, polarization of fibers under the magnetic field increases and microwave attenuation properties enhance as well. Comparing the permittivities of different composites made from ceramic powders pyrolyzed at different temperatures, we can observe that the real permittivity, imaginary permittivity and loss tangent show exponential growth,

Table 2 CoSi, Co content, resistivity, saturation magnetization, coercivity, and ceramic yield of Co–SiC fibers at different treatment temperatures

Pyrolysis temperature (°C)	D_{CoSi} (nm)	Co (wt%)	Resistivity (Ω cm)	Saturation magnetization (emu g^{-1})	Coercivity (G)	Ceramic yield (%)
900	—	1.08	6537.34	0.7653	8.7382	80.65
1000	—	1.11	2881.72	0.3687	24.669	80.55
1100	12.20	1.15	138.21	0.1179	45.609	80.36
1200	14.11	1.22	17.68	0.0062	112.77	80.09

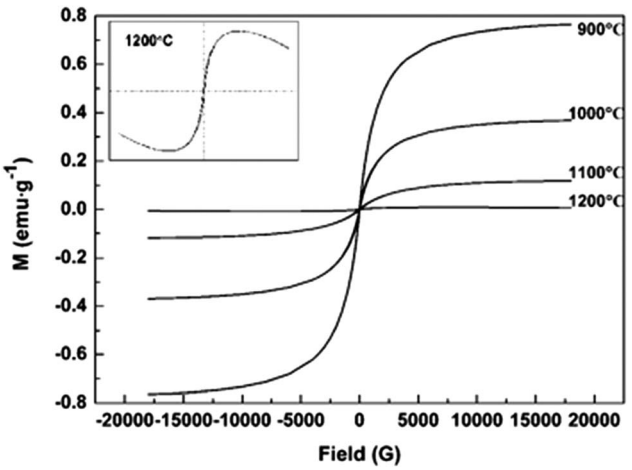

Fig. 10 Hysteresis loop of Co–SiC fibers for curing at 280 °C and pyrolysis from 900 °C to 1200 °C.

suggesting that phases responsible for dielectric loss, such as SiC, C and CoSi, have formed and grown within fibers, leading to bigger growing magnitude of the real permittivity, imaginary permittivity and loss tangent. Therefore, microwave attenuation properties increase with rising temperature.

In order to predict the microwave absorption properties of samples, the reflection coefficient (RC) of the sample is calculated according to the metal back-up panel model using the following equation:[48]

$$\mathrm{RC} = 20\ \log_{10}\left|\frac{Z_{in}-1}{Z_{in}+1}\right| \quad (1)$$

where Z_{in} is the normalized input impedance of the microwave absorption layer, which can be written by the following equation:

$$Z_{in} = \sqrt{\frac{\mu_r}{\varepsilon_r}}\tanh\left[j\frac{2\pi}{c}\sqrt{\mu_r\varepsilon_r}fd\right] \quad (2)$$

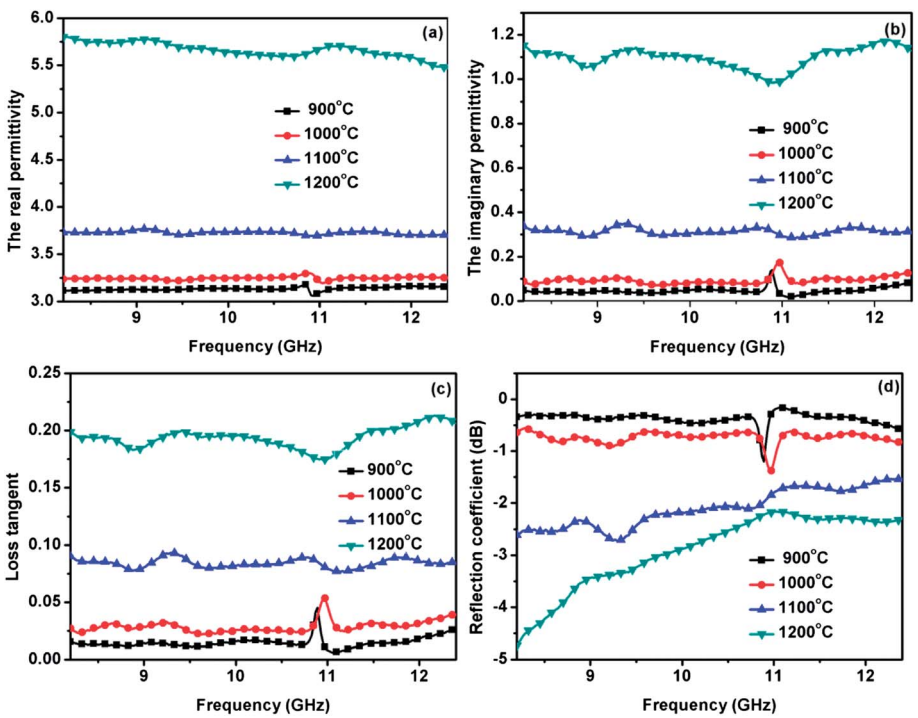

Fig. 11 The relative complex permittivity, loss tangent and reflection coefficient of Co–SiC fibers for curing at 280 °C and pyrolysis from 900 °C to 1200 °C. (a) Real permittivity, (b) imaginary permittivity, (c) loss tangent and (d) reflection coefficient.[49]

where c is the light velocity in a vacuum, d is the thickness of the absorber, and ε_r and μ_r are the relative permittivity and permeability of materials. Owing to the poor magnetic properties of 1% Co–SiC fibers, μ_r is considered to be 1. Therefore, according to eqn (1) and (2), the RC of Co–SiC fibers depends on ε_r and d. The lower RC means the better microwave absorption properties. The RC of Co–SiC fibers with a thickness of 5.0 mm is shown in Fig. 11d. The RC is a key parameter for evaluating wave-absorbing properties of materials. According to the theory of transmission lines, the RC is calculated between 8.2 GHz and 12.4 GHz (X band) for fiber powder/wax composites placed on metal back-up panels. With rising temperature, the RC of composites decreases, indicating that wave-absorbing properties are growing better. Considering that in the composites only ceramic powder absorbs microwave, the wave-absorbing properties of the ceramic powder are elevated with rising temperature.

The tensile strength and Young's modulus of Co–SiC fibers are shown in Fig. 12. Co–SiC fibers reach their highest tensile strength at 1100 °C (1.83 GPa). In general, pure PCS-derived ceramic fibers have the best tensile strength at 1250 °C. The difference may result from the negative effect of Co on the Co–SiC fibers. The decomposition of SiC_xO_y that accompanies the gaseous SiO and CO has adverse effects on the tensile strength. In addition, the extreme growth of β-SiC and CoSi grains has a pivotal function on the decline of strength.

4. Conclusions

We have synthesized a stable Co-colloid *via* the reaction between $Co_2(CO)_8$ and LPCS, which is subsequently added to the spinnable PCS to obtain the Co–PCS precursors. After spinning, oxidation-curing, and pyrolyzing, the Co–SiC fiber is obtained. During the preparation of the Co-colloid, $Co_2(CO)_8$ decomposes into multinucleate carbonyl particles and CO. The LPCS then becomes cross-linked after reacting with the evolved CO, and nanosized carbonyl particles are encapsulated by cross-linked LPCS. The colloid with PCS-bounded Co particles is thus formed. After pyrolyzing at high temperatures, crystalline C, β-SiC, and CoSi are observed in the Co–SiC fiber. The Co–SiC fibers possess the best tensile strength (~1.83 GPa) at 1100 °C. As the pyrolysis temperature increases, the electrical resistivity drops, the loss tangent of Co–SiC fibers increases, and the reflection coefficient (RC) decreases, indicating that microwave attenuation properties increase with the increase of the pyrolysis temperature.

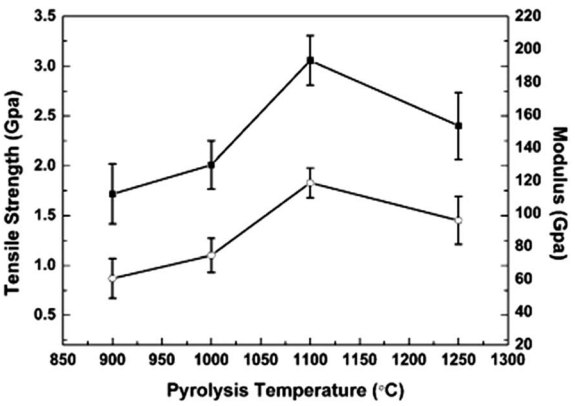

Fig. 12 Tensile strength (○) and Young's modulus (■) as a function of the treatment temperature for Co–SiC fibers (curing at 280 °C).

Acknowledgements

The authors acknowledge the financial support provided by the National Natural Science Foundation of China (no. 51002127 and 51072169) and the helpful discussions with professor Paolo Colombo of several points in the paper. The relative complex permittivity experiments were carried out at Northwestern Polytechnical University (Mainland, China). We thank Prof. Xiaowei Yin and Dr. Fang Ye for their assistance with relative complex permittivity experiments.

References

1 P. Colombo, G. Mera, R. Riedel and G. D. Sorarù, *J. Am. Ceram. Soc.*, 2010, **93**, 1805–1837.
2 S. Yajima, *Philos. Trans. R. Soc., A*, 1980, **294**, 419–426.
3 M. Narisawa, Y. Itoi and K. Okamura, *J. Mater. Sci.*, 1995, **30**, 3401–3406.
4 J. Wang, Y. C. Song and C. X. Feng, *Chin. J. Mater. Res.*, 1998, **12**, 419–422.
5 T. Yamamura, T. Iahikawa and M. Shibuya, *US Pat.*, no. 5094907, 1992.
6 T. Ishikawa, Y. Kohtoku, K. Kumagawa, T. Yamamura and T. Nagasawa, *Nature*, 1998, **391**, 773–775.
7 Z. Y. Chen, X. D. Li, J. Wang and W. F. Li, *Trans. Nonferrous Met. Soc. China*, 2007, **17**, 987–991.
8 J. X. Chen, Ph.D. Thesis, Xiamen University, China, 2007.
9 J. Wang, Y. C. Song and C. X. Feng, *Aerosp. Mater. Technol.*, 1997, **4**, 61–64.
10 A. R. Guo, M. Modesti, J. C. Liu and P. Colombo, *J. Eur. Ceram. Soc.*, 2014, **34**, 549–554.
11 Y. C. Song, J. Wang, J. Liu and C. X. Feng, *J. Mater. Sci. Lett.*, 2003, **22**, 679–681.
12 H. Zhang, W. Ding and D. K. Aidun, *J. Nanosci. Nanotechnol.*, 2014, **14**, 1–9.
13 Z. Y. Chen, X. D. Li, J. Wang and W. F. Li, *Trans. Nonferrous Met. Soc. China*, 2007, **17**, 987–991.
14 D. G. Shin, K. Y. Cho, E. J. Jin and D. H. Riu, *IOP Conf. Ser.: Mater. Sci. Eng.*, 2011, **18**, 082007.
15 Q. Li, X. W. Yin, W. Y. Duan, L. Kong, B. L. Hao and F. Ye, *J. Alloys Compd.*, 2013, **565**, 66–72.
16 M. Zaheer, T. Schmalz, G. Motz and R. Kempe, *Chem. Soc. Rev.*, 2012, **41**, 5102–5116.
17 T. Yajima and H. Kayano, *Nature*, 1976, **264**, 237–238.
18 R. J. P. Corriu, P. Gerbier, C. Guerin and B. Henner, *J. Mater. Chem.*, 2000, **10**, 2173–2182.
19 D. Seyferth, H. Lang, C. A. Sobon, J. Borm, H. J. Tracy and N. Bryson, *J. Inorg. Organomet. Polym. Mater.*, 1992, **2**, 59–77.

20 J. Wang, Y. C. Song and C. X. Feng, *Aerosp. Mater. Technol.*, 1997, **4**, 61–64.
21 D. Seyferth, H. Lang, C. A. Sobon, J. Borm, H. J. Tracy and N. Bryson, *J. Inorg. Organomet. Polym.*, 1992, **2**, 59–77.
22 C. Vakifahmetoglu, P. Colombo, S. M. Carturan, E. Pippel and J. Wotersdorf, *J. Am. Ceram. Soc.*, 2010, **93**, 3709–3719.
23 T. W. Smith, *US Pat.*, US 4252671, 1981, December 4.
24 X. J. Chen, Z. M. Su, L. Zhang, M. Tang, Y. X. Yu, L. T. Zhang, *et al.*, *J. Am. Ceram. Soc.*, 2010, **93**, 89–95.
25 S. Yajima, *Kobunshi*, 1976, **25**, 394–396.
26 M. Birot, E. Bacque, J. P. Pillot and J. Dunogues, *J. Organomet. Chem.*, 1987, **319**, 41–44.
27 S. Yajima, J. Hayashi and M. Omori, *US Pat.*, US 4100233, 1978, July 11.
28 http://www.ch.ntu.edu.tw/~genchem99/doc/T17_Cobalt.pdf.
29 S. Yajima, J. Hayashi and M. Omori, *Chem. Lett.*, 1975, **9**, 931–934.
30 S. Yajima, K. Okamura and J. Hayashi, *Chem. Lett.*, 1975, **12**, 1209–1212.
31 J. W. Cable, R. S. Nyholm and R. K. Sheline, *J. Am. Chem. Soc.*, 1954, **76**, 3373–3376.
32 R. A. Friedel, I. Wender, S. L. Shufler and W. H. Sternberg, *J. Am. Chem. Soc.*, 1955, **77**, 3951–3958.
33 V. Bakumov and E. Kroke, *Langmuir*, 2008, **24**, 10709–10716.
34 T. W. Smith and D. Wychick, *J. Phys. Chem.*, 1980, **84**, 1621–1629.
35 A. H. Lu, E. L. Salabas and F. Schüth, *Angew. Chem., Int. Ed.*, 2007, **46**, 1222–1244.
36 J. S. Yin and Z. L. Wang, *Nanostruct. Mater.*, 1999, **11**, 845–852.
37 R. J. P. Corriu, N. Devylder, C. Guerin, B. Henner and A. Jean, *J. Organomet. Chem.*, 1996, **509**(2), 249–257.
38 K. Okamura, M. Sato and Y. Hasegawa, *J. Mater. Sci. Lett.*, 1983, **2**, 769–771.
39 H. Ichikawa, F. Machino, S. Mitsuno, T. Ishikawa, K. Okamura and Y. Hasegawa, *J. Mater. Sci.*, 1986, **21**, 4352–4358.
40 Y. Hasegawa, M. Iimura and S. Yajima, *J. Mater. Sci.*, 1980, **15**, 720–728.
41 T. Fujimura and S. I. Tanaka, *J. Mater. Sci.*, 1999, **34**, 5743–5747.
42 S. W. Park, Y. I. Kim, J. S. Kwak and H. K. Baik, *J. Electron. Mater.*, 1997, **26**, 172–177.
43 A. R. Bunsell and A. Piant, *J. Mater. Sci.*, 2006, **41**, 823–839.
44 J. Hurst, H. M. Yun and D. Gorican, *Ceram. Trans.*, 1996, **74**, 3–15.
45 F. J. Narciso-Romero and F. Rodriguez-Reinoso, *J. Mater. Sci.*, 1996, **31**, 779–784.
46 J. Wang, Y. C. Song and C. X. Feng, *Mater. Sci. Eng.*, 1998, **16**, 69–71.
47 X. C. Lu, L. F. Chen, S. W. Li, X. Y. Tang, H. Z. Li, L. T. Zhang and M. T. Ding, *J. Funct. Biomater.*, 2014, **45**(7), DOI: 10.3969/j.issn.1001G9731.2014.07.005.
48 Q. Li, X. W. Yin, W. Y. Duan, B. L. Hao, L. Kong and X. M. Liu, *J. Eur. Ceram. Soc.*, 2014, **34**, 589–598.
49 The sharp peaks at 11 GHz of samples pyrolyzed at 900 °C and 1000 °C are due to equipment abnormity, which has not been solved by engineers. The curve now shows a mutation peak at 11 GHz, while it is smooth when the equipment is normal, especially for samples with low dielectric loss. To guarantee the primitiveness of data, we have not done any smoothing to the mutation peaks.